

Peak-time sensitivity kernels for noise cross-correlation envelopes

Bruce D. Cornuelle and Emmanuel K. Skarsoulis

Citation: *The Journal of the Acoustical Society of America* **151**, 2353 (2022); doi: 10.1121/10.0010044

View online: <https://doi.org/10.1121/10.0010044>

View Table of Contents: <https://asa.scitation.org/toc/jas/151/4>

Published by the *Acoustical Society of America*

ARTICLES YOU MAY BE INTERESTED IN

[An overview of array invariant for source-range estimation in shallow water](#)

The Journal of the Acoustical Society of America **151**, 2336 (2022); <https://doi.org/10.1121/10.0009828>

[Modeling underwater sound propagation in an arctic shelf region with an inhomogeneous bottom](#)

The Journal of the Acoustical Society of America **151**, 2297 (2022); <https://doi.org/10.1121/10.0010047>

[Oceanography by ear](#)

The Journal of the Acoustical Society of America **151**, R7 (2022); <https://doi.org/10.1121/10.0009957>

[Extracting Lamb wave vibrating modes with convolutional neural network](#)

The Journal of the Acoustical Society of America **151**, 2290 (2022); <https://doi.org/10.1121/10.0010045>

[Assessing potential perception of shipping noise by marine mammals in an arctic inlet](#)

The Journal of the Acoustical Society of America **151**, 2310 (2022); <https://doi.org/10.1121/10.0009956>

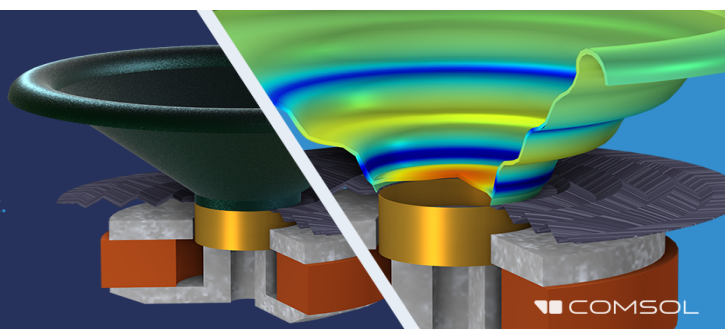
[Human-centered design in acoustics education for undergraduate music majors](#)

The Journal of the Acoustical Society of America **151**, 2282 (2022); <https://doi.org/10.1121/10.0010043>

Take the Lead in Acoustics

The ability to account for coupled physics phenomena lets you predict, optimize, and virtually test a design under real-world conditions – even before a first prototype is built.

» Learn more about COMSOL Multiphysics®



Peak-time sensitivity kernels for noise cross-correlation envelopes

Bruce D. Cornuelle¹  and Emmanuel K. Skarsoulis^{2,a)}

¹Scripps Institution of Oceanography, University of California, San Diego, 9500 Gilman Drive, La Jolla, California 92093-0230, USA

²Institute of Applied and Computational Mathematics, Foundation for Research and Technology Hellas, P.O. Box 1527, 711 10 Heraklion, Crete, Greece

ABSTRACT:

The envelope of the time-lagged cross-correlation of an underwater noise field between two hydrophones can under certain conditions be used as a proxy for active acoustic receptions between the two locations enabling the study of ocean variability. Previous work looked at the sensitivity of cross-correlation peak amplitudes with respect to the distribution of the noise sources. The present study examines the sensitivity of the cross-correlation envelope peak times with respect to changes in the sound-speed distribution. A wave-theoretic scheme allowing for finite-frequency calculations in two and three dimensions, combined with the Born approximation for perturbations of the Green's function and the peak arrival approach, is used to obtain sensitivity kernels with respect to environmental (sound-speed) changes. These kernels provide a way to infer ocean structure from the cross-correlation peaks, considered as observables on their own and valid even in cases where the cross-correlation function does not approximate the time-domain Green's function between the two receivers. The sensitivity behavior is studied for different propagation conditions and noise-source distributions, ranging from spatially distributed uncorrelated noise sources to point sources, such as individual ships. Deviations from linearity are addressed and discussed.

© 2022 Acoustical Society of America. <https://doi.org/10.1121/10.0010044>

(Received 22 December 2021; revised 3 March 2022; accepted 14 March 2022; published online 6 April 2022)

[Editor: Karim G. Sabra]

Pages: 2353–2366

I. INTRODUCTION

Cross-correlation of a noise field between two hydrophones offers a passive way to estimate differential arrival times or channel impulse responses.^{1–4} Under certain conditions, the cross-correlation envelope approximates the envelope of the time-domain acoustic pressure at one location due to an active broadband source at another location,^{5–9} the so-called arrival pattern. The essential contributions to the cross-correlation function are due to the noise components that travel coherently through both receiver locations, i.e., travel along acoustic paths (eigenrays) connecting the two locations. Thus, the part of the arrival pattern that can be recovered is mainly determined by the directivity of the noise field and the stimulation of the connecting paths; the noise contributions along a connecting path add up coherently and gradually emerge from the incoherent noise background.^{10–12}

The arrival pattern at one location due to an acoustic source at another location results from the convolution of the channel impulse response with the transmitted pulse. Ocean acoustic tomography¹³ exploits the sensitivity of the travel times between a controlled source and a receiver to sound-speed perturbations to estimate the ocean state from arrival-time measurements. In this connection, the travel-time sensitivity kernels (TSKs), spatial functions quantifying the sensitivity of active transmission peak arrival times

to the location and strength of sound-speed perturbations, have been introduced.^{13,14} The central frequency and bandwidth of the emitted signals are critical for the resolution and the spatial sensitivity of the travel-time observables.^{13,15}

The possibility of recovering the active arrival pattern through the noise cross-correlation envelope opens the way for passive environmental monitoring, using ambient noise and bypassing the need for active sources.^{16–19} However, the efficiency of such an approximation critically relies on the directivity of the noise field, which in turn, depends on the distribution of noise sources and the propagation conditions.^{20–23} The sensitivity of the cross-correlation amplitude to the noise-source distribution and the refractive characteristics of the environment can be used to assess the feasibility of a passive proxy to the arrival pattern for particular types of noise sources in a particular environment.²⁴

Realistic noise fields are, in general, inhomogeneous and anisotropic, because of the non-uniform distribution of noise sources and because of acoustic refraction taking place in the water column.^{20–23} Ship noise sources, for example, are localized in space and time and their cross-correlations may not average away quickly. Furthermore, refraction has a significant impact and gives rise to directivity of the induced noise field, even if the underlying noise sources are omni-directional. Consequently, the receiver-to-receiver arrival pattern cannot always be fully recovered from the cross-correlation envelope.¹² Nevertheless, even in cases where the arrival pattern cannot be recovered, the cross-

^{a)}Electronic mail: eskars@iacm.forth.gr

correlation envelope, and particularly its peaks, convey information about the environment and can be used as observables.

The present work aims to generalize the utility of observations of noise cross-correlation, independently of its relation to the time-domain Green's function (TDGF), by providing a framework for calculating the sensitivity of cross-correlation envelope peak times to sound-speed changes. Quantifying the peak times through a wave-theoretic representation for the Green's function and using the Born approximation for perturbations of the latter, the cross-correlation peak-time sensitivity kernels (CTSKs) are derived. Then, using this tool, the sensitivity of cross-correlation envelope peak times is studied for different propagation conditions and noise-source distributions, ranging from spatial distributions of uncorrelated noise sources to point sources, such as individual ships.

The dependence of peak times on sound-speed changes is non-linear in general. The CTSKs describe the first-order (linear) term in the Taylor expansion of peak-time perturbations as a function of the underlying sound-speed perturbations about the reference state. From a ray-theoretic perspective, the peak times in the cross-correlation envelope are the time differences between eigenrays connecting the two receivers with the noise source(s), and the CTSKs are concentrated around the corresponding eigenrays. In the case of finite-bandwidth receptions, the time resolution of the arrival peaks is limited, so multiple rays may contribute to a single observed peak in the arrival pattern or the cross-correlation envelope. In this case, the wave-theoretic approach is a quantitative way to calculate the sensitivity of the peak arrival time, but the region of linearity may be small due to interference effects between the unresolved ray arrivals.

The CTSKs can be considered as the passive counterparts of the TSKs. While the TSKs describe the sensitivity with respect to sound-speed changes of peak arrival times, defined on the arrival pattern at one location due to an active source at another location, the CTSKs deal with the peak times (time lags) defined on the cross-correlation envelope of a diffuse noise field at the two locations. This work extends two previous works, one introducing a wave-theoretic scheme for the calculation of the noise cross-correlation function¹² and one describing the sensitivity of the cross-correlation function on the noise source distribution taking into account refraction.²⁴ The same sample problems and assumed environments from those works are adopted here to simplify comparisons, although the present method can be applied to more general noise source distributions and environments, including range dependence.

The contents of the work are organized as follows. In Sec. II, the cross-correlation peak-time sensitivity kernel is derived based on the wave-theoretic description of the cross-correlation function in terms of the Green's function, the Born approximation for perturbations of the latter, and the peak arrival approach for the definition of peak times. The derivation benefits from the analytic representation of the time-domain

acoustic pressure and the cross-correlation function addressed in the Appendix. In Sec. III, numerical results are presented for CTSKs in representative environments with various noise source distributions, as well as results addressing the deviations from linearity in the dependence between peak times and sound-speed changes. Finally, a discussion and basic conclusions are presented in Sec. IV.

II. PEAK-TIME SENSITIVITY KERNELS

In this section, the expression for the sensitivity kernel of the peak times of the noise cross-correlation envelope is derived. As shown in the Appendix, the cross-correlation envelope can be expressed as the modulus of the complex-valued cross-correlation resulting from the analytic representation of the acoustic pressure in the time domain.

Assuming a stationary noise field $p(t; \mathbf{x})$, which is a random real-valued function of time t and space \mathbf{x} , with analytic representation $p_a(t; \mathbf{x})$, such that $\Re\{p_a(t; \mathbf{x})\} = p(t; \mathbf{x})$, the complex-valued cross-correlation function between locations \mathbf{x}_1 and \mathbf{x}_2 can be expressed by the Wiener–Khintchine theorem^{25,26} as follows:

$$\begin{aligned}\psi_{1,2}(\tau) &= \langle p_a(t + \tau; \mathbf{x}_1) p_a^*(t; \mathbf{x}_2) \rangle \\ &= \frac{1}{2\pi} \int_{-\infty}^{\infty} \langle P_a(\omega; \mathbf{x}_1) P_a^*(\omega; \mathbf{x}_2) \rangle e^{i\omega\tau} d\omega,\end{aligned}\quad (1)$$

where τ denotes time lag, ω circular frequency, $\langle \rangle$ expectation, $*$ complex conjugation, and P_a is the frequency-domain counterpart (the Fourier transform) of p_a .

Assuming a distribution $N(\omega; \mathbf{x}_s)$ of noise sources over a volume V , the complex pressure P_a in the frequency domain at location \mathbf{x}_r can be expressed through the representation theorem as

$$P_a(\omega; \mathbf{x}_r) = \int_{\mathbf{x}_s} G_+(\omega; \mathbf{x}_r | \mathbf{x}_s) H(\omega) N(\omega; \mathbf{x}_s) dV(\mathbf{x}_s), \quad (2)$$

where $H(\omega)$ is the receiver transfer function supported on the corresponding receiving bandwidth. G_+ is the one-sided, frequency-domain Green's function, cf. Eq. (A4) in the Appendix, given by

$$G_+(\omega; \mathbf{x}_r | \mathbf{x}_s) = \begin{cases} 2G(\omega; \mathbf{x}_r | \mathbf{x}_s) & \text{for } \omega > 0 \\ 0 & \text{for } \omega < 0,\end{cases} \quad (3)$$

where $G(\omega; \mathbf{x}_r | \mathbf{x}_s)$ is the two-sided Green's function, which is Hermitian, i.e., $G(\omega; \mathbf{x}_r | \mathbf{x}_s) = G^*(-\omega; \mathbf{x}_r | \mathbf{x}_s)$, giving a real-valued acoustic pressure p in the time domain.

Assuming a spatially uncorrelated distribution of isotropic noise sources

$$\langle N(\omega; \mathbf{x}_s) N^*(\omega; \mathbf{x}'_s) \rangle = S(\omega; \mathbf{x}_s) \delta(\mathbf{x}_s - \mathbf{x}'_s), \quad (4)$$

where $S(\omega; \mathbf{x}_s)$ is the space-frequency distribution of the anticipated noise spectral density, the cross-correlation $\psi_{1,2}(\tau)$ can be written as

$$\begin{aligned} \psi_{1,2}(\tau) &= \frac{1}{2\pi} \int_{\mathbf{x}_s} \int_{\omega} H_1(\omega) H_2^*(\omega) S(\omega; \mathbf{x}_s) \\ &\times G_+(\omega; \mathbf{x}_1 | \mathbf{x}_s) G_+^*(\omega; \mathbf{x}_2 | \mathbf{x}_s) e^{i\omega\tau} d\omega dV(\mathbf{x}_s), \end{aligned} \quad (5)$$

where $H_1(\omega)$ and $H_2(\omega)$ is the transfer function of the receivers at locations \mathbf{x}_1 and \mathbf{x}_2 , respectively. A perturbation $\delta c(\mathbf{x})$ in the sound-speed distribution $c(\mathbf{x})$ will result in a perturbation δG_+ of the Green's function which to the first order is given by the Born approximation^{27,28}

$$\begin{aligned} \delta G_+(\omega; \mathbf{x}_1 | \mathbf{x}_2) &= -\omega^2 \int_{\mathbf{x}} G_+(\omega; \mathbf{x} | \mathbf{x}_2) G_+(\omega; \mathbf{x}_1 | \mathbf{x}) \\ &\times \frac{\delta c(\mathbf{x})}{c^3(\mathbf{x})} dV(\mathbf{x}). \end{aligned} \quad (6)$$

While in the standard Born approximation, there is an additional factor of 2, in the above expression for the one-sided Green's function G_+ , defined as in Eq. (3), this factor is absent. Eqs. (5) and (6) can be used to obtain the expression for the first-order perturbation of the cross-correlation function $\delta\psi_{1,2}$,

$$\begin{aligned} \delta\psi_{1,2}(\tau) &= \frac{1}{2\pi} \int_{\mathbf{x}_s} \int_{\omega} H_1(\omega) H_2^*(\omega) S(\omega; \mathbf{x}_s) [\delta G_+(\omega; \mathbf{x}_1 | \mathbf{x}_s) \\ &\times G_+^*(\omega; \mathbf{x}_2 | \mathbf{x}_s) + G_+(\omega; \mathbf{x}_1 | \mathbf{x}_s) \delta G_+^*(\omega; \mathbf{x}_2 | \mathbf{x}_s)] \\ &\times e^{i\omega\tau} d\omega dV(\mathbf{x}_s) \\ &= -\frac{1}{2\pi} \int_{\mathbf{x}} \frac{\delta c(\mathbf{x})}{c^3(\mathbf{x})} dV(\mathbf{x}) \int_{\omega} H_1(\omega) H_2^*(\omega) \omega^2 e^{i\omega\tau} d\omega \\ &\times \left\{ G_+(\omega; \mathbf{x}_1 | \mathbf{x}) \int_{\mathbf{x}_s} G_+(\omega; \mathbf{x} | \mathbf{x}_s) G_+^*(\omega; \mathbf{x}_2 | \mathbf{x}_s) \right. \\ &\times S(\omega; \mathbf{x}_s) dV(\mathbf{x}_s) + G_+^*(\omega; \mathbf{x}_2 | \mathbf{x}) \\ &\left. \times \int_{\mathbf{x}_s} G_+^*(\omega; \mathbf{x} | \mathbf{x}_s) G_+(\omega; \mathbf{x}_1 | \mathbf{x}_s) S(\omega; \mathbf{x}_s) dV(\mathbf{x}_s) \right\}. \end{aligned} \quad (7)$$

The cross-correlation envelope is defined as the modulus of $\psi_{1,2}$,

$$a_{1,2}(\tau) = |\psi_{1,2}(\tau)| = \sqrt{v_{1,2}^2(\tau) + w_{1,2}^2(\tau)}, \quad (8)$$

where $v_{1,2}(\tau)$ and $w_{1,2}(\tau)$ are the real and imaginary parts of the complex-valued cross-correlation function, respectively, $\psi_{1,2}(\tau) = v_{1,2}(\tau) + iw_{1,2}(\tau)$.

The peak times of the cross-correlation envelope are the time lags corresponding to its local maxima, thus satisfying the condition $\dot{a}_{1,2}(\tau) = 0$, where a dot denotes time differentiation. For convenience, the squared envelope $A_{1,2}(\tau) = a_{1,2}^2(\tau) = v_{1,2}^2 + w_{1,2}^2$ is considered in the following, with the peak times satisfying the condition $\dot{A}_{1,2}(\tau) = 0$. The peak-time perturbations in $a_{1,2}(\tau)$ and $A_{1,2}(\tau)$ will be the same.

A perturbation of the squared cross-correlation envelope will lead to a perturbation of the above-defined peak times, which to the first order is given by the expression²⁹

$$\delta\tau = -\frac{\delta\dot{A}_{1,2}(\tau)}{\ddot{A}_{1,2}(\tau)}. \quad (9)$$

Based on the definition of $A_{1,2}$, its perturbation and time derivatives can be expressed in terms of perturbations and derivatives of the real and imaginary parts $v_{1,2}(\tau)$ and $w_{1,2}(\tau)$ of the cross-correlation function $\psi_{1,2}$. In the following, the dependence on the peak time τ is omitted for brevity:

$$\begin{aligned} \dot{A}_{1,2} &= 2(v_{1,2}\dot{v}_{1,2} + w_{1,2}\dot{w}_{1,2}), \\ \ddot{A}_{1,2} &= 2(\dot{v}_{1,2}^2 + v_{1,2}\ddot{v}_{1,2} + \dot{w}_{1,2}^2 + w_{1,2}\ddot{w}_{1,2}) = 2b, \\ \delta\dot{A}_{1,2} &= 2(\dot{v}_{1,2}\delta v_{1,2} + v_{1,2}\delta\dot{v}_{1,2} + \dot{w}_{1,2}\delta w_{1,2} + w_{1,2}\delta\dot{w}_{1,2}). \end{aligned} \quad (10)$$

Combination of the above leads to the following alternative expressions for the peak-time perturbation

$$\begin{aligned} \delta\tau &= -\frac{1}{b} (\dot{v}_{1,2}\delta v_{1,2} + v_{1,2}\delta\dot{v}_{1,2} + \dot{w}_{1,2}\delta w_{1,2} + w_{1,2}\delta\dot{w}_{1,2}) \\ &= -\frac{1}{b} \Re \left\{ (\dot{v}_{1,2} - i\dot{w}_{1,2}) \delta\psi_{1,2} + (v_{1,2} - iw_{1,2}) \delta\dot{\psi}_{1,2} \right\} \\ &= -\frac{1}{b} \Re \left\{ \dot{\psi}_{1,2}^* \delta\psi_{1,2} + \psi_{1,2}^* \delta\dot{\psi}_{1,2} \right\} \\ &= -\frac{1}{b} \Re \left\{ \frac{\partial}{\partial\tau} [\psi_{1,2}^* \delta\psi_{1,2}] \right\}. \end{aligned} \quad (11)$$

By combining Eq. (11), relating peak-time perturbations to perturbations of the cross-correlation function, with Eq. (7), relating the latter to the underlying sound-speed perturbations, a perturbation relation between travel-time and sound-speed perturbations can be obtained of the form

$$\delta\tau = \int_{\mathbf{x}} K_{1,2}(\mathbf{x}; \tau) \delta c(\mathbf{x}) dV(\mathbf{x}), \quad (12)$$

where the kernel $K_{1,2}(\mathbf{x}; \tau)$ is given by the expression

$$\begin{aligned} K_{1,2}(\mathbf{x}; \tau) &= \frac{1}{b(\tau)c^3(\mathbf{x})} \Re \left\{ \frac{1}{2\pi} \int_{\omega} H_1(\omega) H_2^*(\omega) \omega^2 \right. \\ &\times \left[\dot{\psi}_{1,2}^*(\tau) + i\omega\psi_{1,2}^*(\tau) \right] \\ &\times \left[G_+(\omega; \mathbf{x}_1 | \mathbf{x}) \int_{\mathbf{x}_s} G_+(\omega; \mathbf{x} | \mathbf{x}_s) G_+^*(\omega; \mathbf{x}_2 | \mathbf{x}_s) \right. \\ &\times S(\omega; \mathbf{x}_s) dV(\mathbf{x}_s) + G_+^*(\omega; \mathbf{x}_2 | \mathbf{x}) \\ &\left. \times \int_{\mathbf{x}_s} G_+^*(\omega; \mathbf{x} | \mathbf{x}_s) G_+(\omega; \mathbf{x}_1 | \mathbf{x}_s) \right. \\ &\left. \times S(\omega; \mathbf{x}_s) dV(\mathbf{x}_s) \right] e^{i\omega\tau} d\omega \right\}. \end{aligned} \quad (13)$$

This is the cross-correlation peak-time sensitivity kernel (CTSK), different for each peak, describing the effects that a sound-speed perturbation at any location \mathbf{x} will have on the corresponding peak time τ . In the expression of the right side of Eq. (13), the dependences on the time τ , i.e., those of ψ and b , are explicitly expressed for clarity.

III. NUMERICAL RESULTS

Some numerical results are presented in this section to illustrate the noise cross-correlation function and the

corresponding peak-time sensitivity kernels. All cases use a deep-water environment, with water depth of 2500 m and fully absorbing bottom (bottom sound speed and density equal to that of the water at the interface) such that the focus is on propagation in the water column.

A. 2D CTSKs—Linear SVP

The first example uses a linear sound-velocity profile (SVP), 1503 m/s at the surface and 1547 m/s at 2500 m depth, the upper 800 m of which is shown in Fig. 1(a). This corresponds roughly to uniform temperature in the water column and represents typical winter conditions in the Mediterranean Sea. Figure 1(b) shows the waterborne eigenrays connecting two locations, A and B, at 150 m depth and separated by 20 km. Figure 1(c) shows the corresponding ray arrivals at location B due to a source at location A. There are six eigenrays but five distinct ray arrivals with arrival times between 13.25 and 13.3 s. The first and weakest arrival results from the deepest (refracted only) acoustic path encountering the largest sound-speed values. The second arrival is a double arrival from two symmetric eigenrays with one surface reflection each. Finally, the last/strongest arrival corresponds to the shallowest acoustic path with two surface bounces, seeing the smallest sound-speed values.

The top panel of Fig. 2 shows the wave-theoretic arrival pattern, i.e., the modulus of the complex pressure in the time domain, normalized to have maximum amplitude of 1, at location B due to a source at location A emitting a Gaussian pulse of central frequency 100 Hz and 3-dB bandwidth 70 Hz, calculated using the 2-dimensional (2D) normal-mode representation for the Green's function in the frequency domain.³⁰ For the wave-theoretic calculations, the KRAKEN normal-mode code³¹ is used. The three peak arrivals correspond to the convolution of the ray arrivals of Fig. 1(c)—also shown here for comparison purposes—with the emitted Gaussian pulse and convey information from different depth layers. The lower panels in Fig. 2 show the

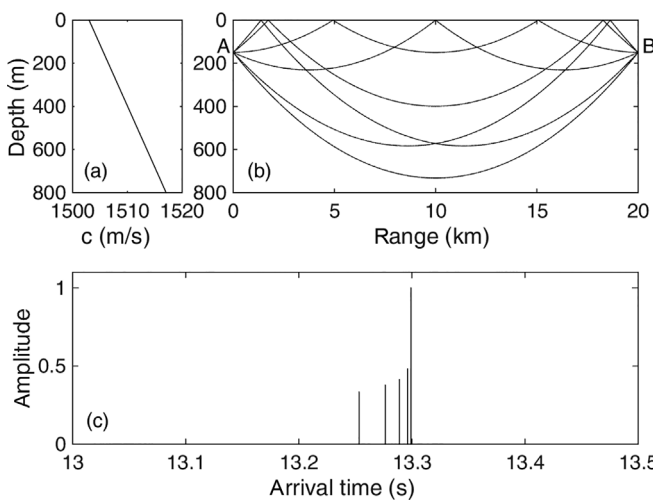


FIG. 1. (a) Linear SVP, shown in the upper 800 m. (b) Eigenrays connecting a source and a receiver at 150-m depth and 20 km apart. (c) Ray-theoretic arrival pattern.

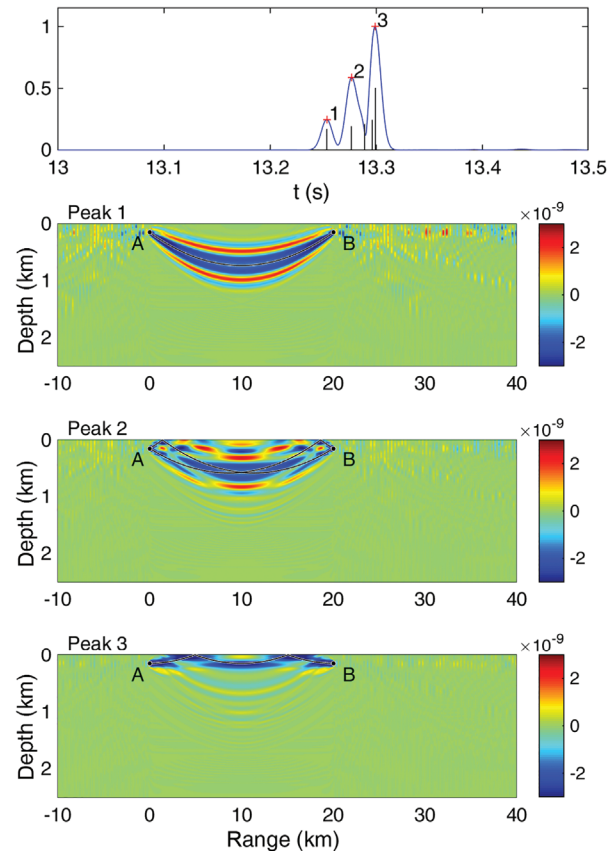


FIG. 2. Top panel: Normalized wave-theoretic 2D arrival pattern at location B (blue) due to a Gaussian source of central frequency 100 Hz and 3-dB bandwidth 70 Hz at A (linear SVP) with superposed ray-theoretic arrival pattern in black. Lower panels: 2D travel-time sensitivity kernels ($s^2 m^{-3}$) and corresponding eigenrays (black lines) for peaks 1, 2, and 3 marked in the top panel.

2D travel-time sensitivity kernels (TSKs), along with the corresponding eigenrays, for the three marked peaks, labeled 1, 2, and 3, respectively, revealing the areas where a sound-speed change will affect the corresponding travel times.¹⁴

The sensitivity kernel for the first peak arrival time is strongest near the deepest (refracted only) eigenray path, where it has negative sensitivity, represented by the blue color, surrounded by alternating positive and negative sensitivity zones associated with Fresnel zones³²—the Fresnel radius at mid-range (10 km) for a frequency of 100 Hz is 194 m. While the width of the sensitivity core and the surrounding zones is governed by the source frequency—it decreases with frequency¹⁴—the overall kernel width depends on the source bandwidth—it decreases with bandwidth.¹⁵ The noise appearing away from the main sensitivity domains is of numerical origin due to mode interference. The sensitivity kernel for the second peak arrival time corresponds to the interference of two acoustic paths giving rise to a more complicated interference pattern. Finally, the kernel for the last peak arrival time corresponds to the shallowest eigenray. In all cases, the negative sensitivity dominates, reflecting the fact that a sound-speed increase leads to a travel-time decrease.

The active arrival pattern of Fig. 2 between A and B can be recovered through noise cross-correlation between the two locations. The top panel of Fig. 3 shows the normalized 2D cross-correlation envelope between locations A and B, at 150 m depth and 20 km apart, of the noise field generated by a near-surface uniform distribution of noise sources at 10 m depth and ranges from 31 to 100 km from A (11–80 km from B), partially shown in red in the lower panels of Fig. 3, assuming a Gaussian form for the receiving filter, the product $H_1(\omega)H_2^*(\omega)$ in Eqs. (5) and (13), centered at 100 Hz and with 3-dB bandwidth 70 Hz, same as the central frequency and bandwidth of the emitted pulse in the previous active case. It is seen that the time-lagged cross-correlation envelope in Fig. 3 is a very good approximation of the arrival pattern of Fig. 2: the time lags corresponding to the envelope peaks match the arrival times to nanosecond accuracy, and the normalized peak amplitudes have a relative root-mean-square (RMS) deviation of 3.8%. The good agreement between the arrival pattern and the cross-correlation envelope is due to the propagation conditions in this case which lead to a favorable directivity pattern of the induced noise field at the two receiver locations concentrated about the horizontal, which in turn, excites all acoustic paths connecting the two locations A and B.¹²

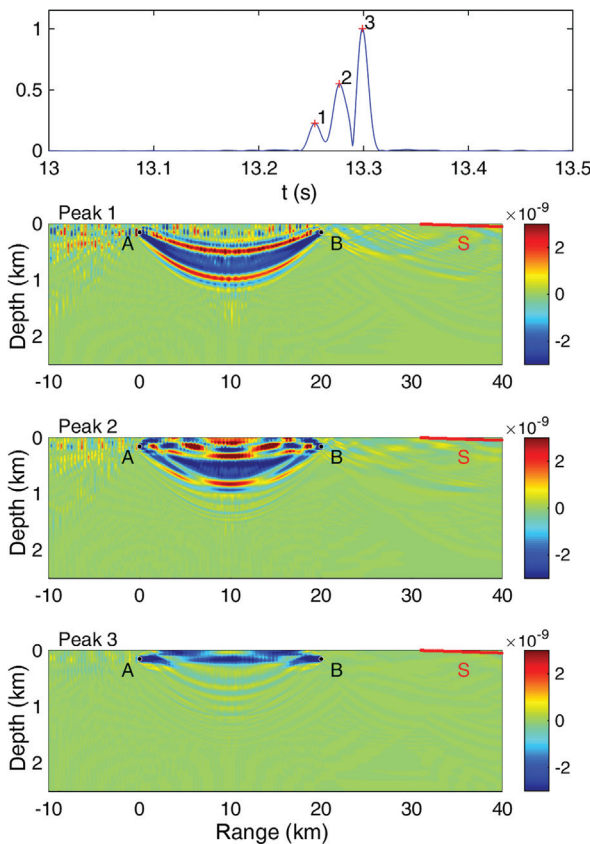


FIG. 3. Top panel: Normalized 2D cross-correlation envelope at two receivers A and B located at 150-m depth and separated by 20 km with Gaussian receiving filters centered at 100 Hz and with 3-dB bandwidth 70 Hz due to uncorrelated noise sources at 10 m depth and ranges from 31 to 100 km (linear SVP). Lower panels: 2D peak-time sensitivity kernels (s^2m^{-3}) for peaks 1, 2, and 3 marked in the top panel. The noise source (S) distribution is marked in red.

The lower panels of Fig. 3 show the 2D cross-correlation peak-time sensitivity kernels (CTSKs) for the peaks marked on the cross-correlation envelope in the top panel. They too are good approximations of the TSKs shown in Fig. 2, both in shape and magnitude; the TSK and the CTSK units in the 2D case are s^2m^{-3} , in agreement with Eq. (12), taking into account that the elementary 2D volume is in m^2 , the time lag in seconds, and the sound-speed perturbation in m/s. The agreement between the TSKs and the CTSKs might be expected using the argument that if the cross-correlation is a good approximation of the arrival pattern, then the corresponding TSKs and CTSKs should agree as well. On the other hand, the noise cross-correlation function and the corresponding peak times also depend on propagation conditions in the outer domain reaching out to the location of the noise sources. In this connection, one might also expect sensitivity to sound-speed variations not only between the two receivers but also in the direction of the noise sources. This is observed in the 3D CTSK results presented below.

B. 3D CTSKs—Linear SVP

Figure 4 presents the 3-dimensional (3D) noise cross-correlation envelope and the corresponding CTSKs between the locations A and B, based on the normal-mode representation of the 3D Green's function,³⁰ for a horizontal line of uncorrelated noise sources in the endfire direction, i.e., on the same vertical plane as the two receivers, at 10 m depth and ranges from 31 to 100 km from A, shown in the lower panels in red. The lower panels show cross sections of the 3D CTSKs on the vertical plane through A and B. The units of the 3D CTSK are s^2m^{-4} , since the elementary 3D volume in Eq. (12) is in m^3 , whereas the time lag and the sound-speed perturbation are in seconds and m/s, respectively. The receiver geometry and frequency characteristics are the same as before.

While the 2D and 3D noise cross-correlation envelopes are almost identical—peak time and relative peak amplitude RMS deviations of 0.28 ms and 5.4%, respectively—the 2D and 3D CTSKs exhibit significant differences. Between the two receivers, the 3D CTSKs are concentrated about the corresponding eigenrays, as in the 2D case; nevertheless, the maximum negative sensitivity occurs at a distance from the eigenray, not on the eigenray. This is clearly observed in the CTSK of the first peak corresponding to a single eigenray. This corresponds to a well-known difference between 3D and 2D travel-time sensitivity kernels.^{32–34} In the outer region, the 3D CTSKs in Fig. 4 exhibit significant sensitivities between receiver B and the noise sources, which are not observed in the 3D TSK (not shown here) nor in the 2D CTSKs of Fig. 3. These sensitivities are possibly associated with changes in the noise field at the two receivers due to changes in the propagation conditions between the receivers and the noise sources, which, in turn, may affect the cross-correlation output.

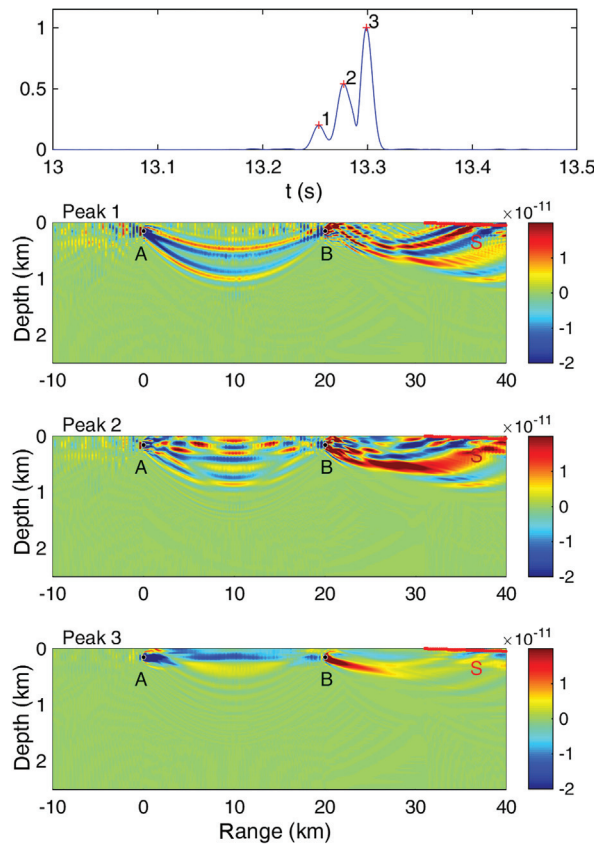


FIG. 4. Top panel: Normalized 3D cross-correlation envelope at two receivers A and B located at 150-m depth and separated by 20 km with Gaussian receiving filters centered at 100 Hz and with 3-dB bandwidth 70 Hz due to a horizontal line of uncorrelated noise sources at 10 m depth and ranges from 31 to 100 km in the endfire direction (linear SVP). Lower panels: Cross sections of 3D peak-time sensitivity kernels ($s^2 m^{-4}$) on the vertical plane through the two receivers for peaks 1, 2, and 3 marked in the top panel. The noise source (S) distribution is marked in red.

Figure 5 shows transversal cross sections of the 3D CTSKs for the three peaks marked in Fig. 4 at ranges of 10 km, i.e., in the middle between the two receivers (upper three panels), and 30 km, i.e., in the outer domain (lower three panels). The CTSKs between the receivers exhibit the well-known Fresnel-zone structure with alternating negative and positive sensitivities extending up to about 500 m from the vertical plane through the receivers. In the outer domain, the 3D CTSKs also exhibit positive and negative sensitivities forming more complicated patterns supported within about 1000 m from the central vertical plane through the receivers.

For cases where the horizontal scale of the ocean perturbations is larger than the cross-range extent of the 3D kernels, the horizontal cross-range marginals of the latter can be used to describe the resulting sensitivity distribution. Figure 6 presents the horizontal cross-range marginals of the 3D CTSKs for the peaks marked in Fig. 4. For this calculation, the 3D CTSKs have been integrated horizontally cross-range over 2 km relative to the central vertical plane through the receivers with 5-m step. Interestingly, the marginalization leads to a suppression of the sensitivities

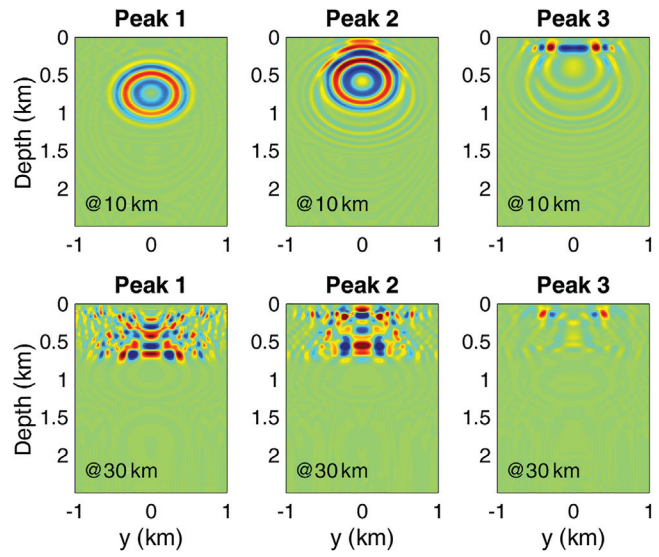


FIG. 5. Vertical transverse cross sections of 3D peak-time sensitivity kernels ($s^2 m^{-4}$) of Fig. 4 at a range of 10 km, i.e., at mid-range between the two receivers A and B (top) and at a range of 30 km (bottom) for the peaks marked in Fig. 4 using the same color scale.

observed in Fig. 4 outside the two receivers, A and B. The cross-range integration has averaged out the alternating sensitivities in the outer region, resulting in near-zero sensitivity there, similar to the 2D CTSKs. Further, the marginal 3D CTSKs between the two receivers closely match the corresponding 2D CTSKs and TSKs of Figs. 3 and 2, respectively.

In the rest of the cases, only 2D results will be shown. While the 3D structures are likely important in many cases, they are not central to the analysis here.

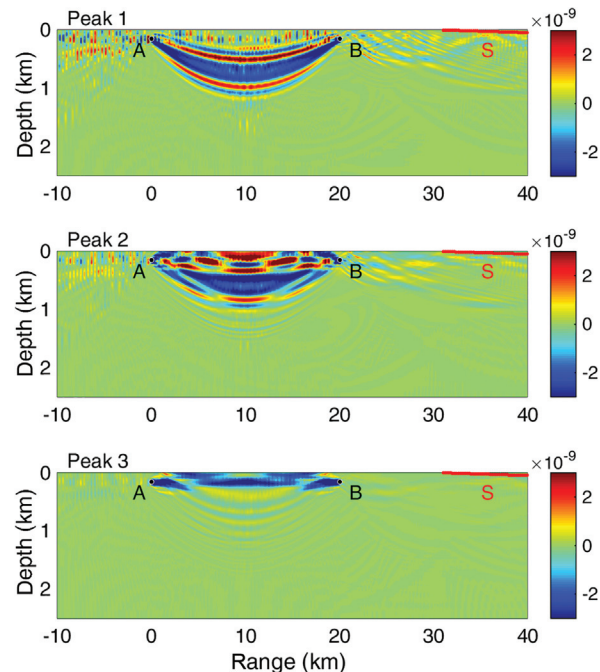


FIG. 6. Marginals, with respect to the horizontal cross-range dimension, of 3D peak-time sensitivity kernels of Figs. 4 and 5 for the peaks marked in Fig. 4. The units are $s^2 m^{-3}$. The noise source (S) distribution is marked in red.

C. 2D CTSKs–Bilinear SVP

In the previous examples in Secs. III A and III B, the noise cross-correlation envelope offered a good approximation of the arrival pattern for propagation between the receiver locations because the propagation conditions resulted in noise directivity patterns which could excite all ray paths connecting the two locations A and B. In other words, the eigenrays between the two receivers all continued onto and interacted with the sea surface and thus, could be sufficiently excited by the near-surface noise source distribution. In such a case, the noise cross-correlation envelopes and the corresponding CTSKs can be seen as proxies to the active arrival patterns and the TSKs, respectively. However, this may not be true if some of the eigenrays or their extensions remain far from the sea surface and do not connect to the noise sources. Such a situation arises in the case of a bilinear sound-speed profile addressed below.

The bilinear sound-speed profile shown in Fig. 7(a) is the same as that in Fig. 1(a) below 100 m but linearly increases to 1511 m/s at the surface. Figure 7(b) shows the waterborne eigenrays connecting locations A and B separated by 20 km at 150 m depth. It is seen that in contrast to the previous case (linear SVP), some of the rays have upper turning points more than 50 m below the surface. The corresponding ray arrivals are shown in Fig. 7(c). While the first arrival time corresponding to the deep eigenray remains unchanged, the later arrivals of eigenrays interacting with the upper 100 m layer are advanced due to the sound-speed increase, leading to a more contracted arrival pattern.

Figure 8 shows the normalized wave-theoretic 2D arrival pattern and the corresponding TSKs for the three marked peaks at location B due to a Gaussian pulsed source at location A of central frequency 100 Hz and 3-dB bandwidth 140 Hz. The higher bandwidth (140 Hz) was used to separate arrivals 2 and 3 since they are closer to each other because of the contraction of the arrival pattern and would otherwise overlap with each other. Superposed on Fig. 8 are

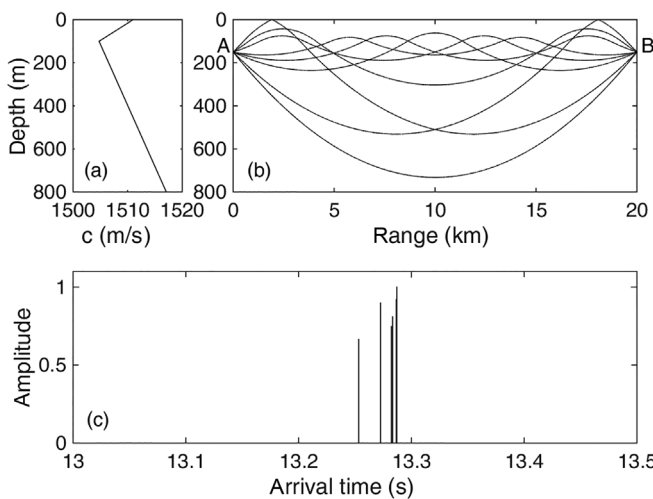


FIG. 7. (a) Bilinear SVP, shown in the upper 800 m. (b) Eigenrays connecting a source and a receiver at 150-m depth and 20 km apart. (c) Ray-theoretic arrival pattern.

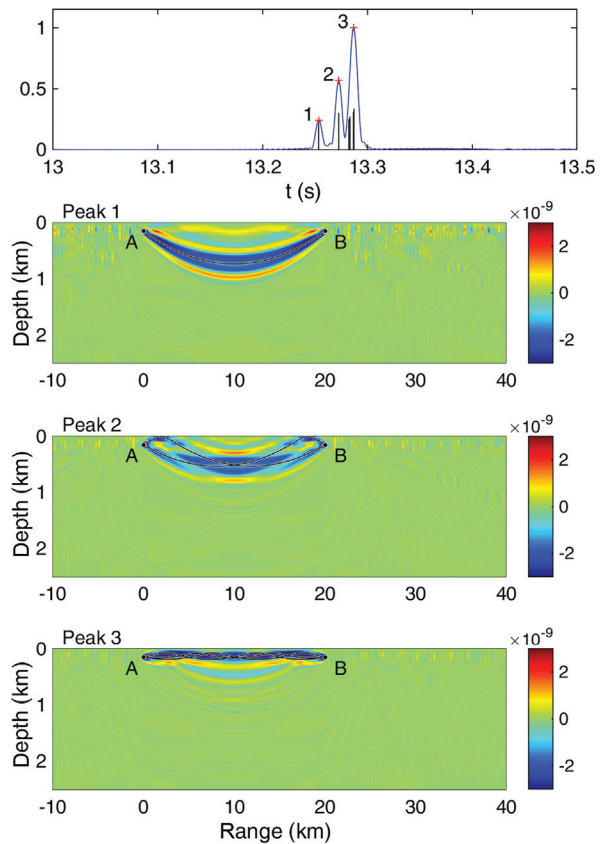


FIG. 8. Top panel: Normalized wave-theoretic 2D arrival pattern at location B (blue) due to a Gaussian source of central frequency 100 Hz and 3-dB bandwidth 140 Hz at A (bilinear SVP) with superposed ray-theoretic arrival pattern in black. Lower panels: 2D travel-time sensitivity kernels ($s^2 m^{-3}$) and corresponding eigenrays (black lines) for peaks 1, 2, and 3 marked in the top panel.

the ray arrivals in the top panel and the corresponding eigenrays in the lower panels. While the TSKs of peaks 1 and 2 are of similar shape as in Fig. 2—albeit with slightly smaller overall kernel width due to the larger bandwidth—the TSK for peak 3 retains some distance from the sea surface being associated with eigenrays with upper turning points at 60–80 m below the surface, as shown in the bottom panel. Thus, also the extensions of these eigenrays will not interact with the sea surface, and because of this one would expect a weaker excitation of the corresponding cross-correlation peaks by near-surface noise sources.

This is seen in Fig. 9 which presents the 2D noise cross-correlation envelope between locations A and B and the corresponding CTSKs due to a distribution of near-surface noise sources at 10 m depth and ranges between 31 and 100 km from A, partially shown in the lower panels in red, subject to Gaussian filtering with the same central frequency (100 Hz) and bandwidth (140 Hz) as those of the active pulse. The cross-correlation envelope in the upper panel is normalized to the scale of the first peak arrival in Fig. 8, such that the first arrivals in Figs. 8 and 9 have the same amplitude. With this normalization, the second and third cross-correlation peaks are weaker by 21% and 74%, respectively, compared to the second and third arrivals in Fig. 8.

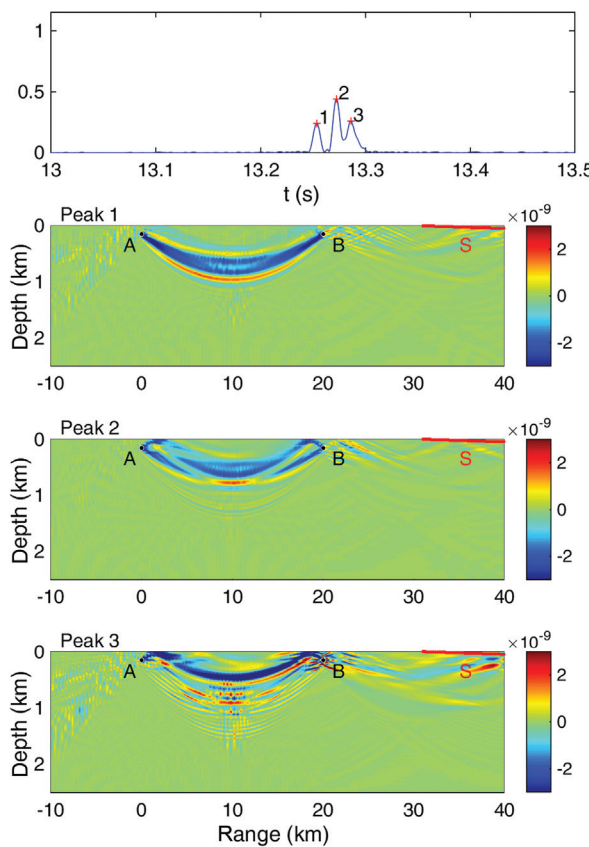


FIG. 9. Top panel: Normalized 2D cross-correlation envelope at two receivers A and B located at 150-m depth and separated by 20 km with Gaussian receiving filters centered at 100 Hz and with 3-dB bandwidth 140 Hz due to uncorrelated noise sources at 10-m depth and ranges from 31 to 100 km (bilinear SVP). Lower panels: 2D peak-time sensitivity kernels ($s^2 m^{-3}$) for peaks 1, 2, and 3 marked in the top panel. The noise source (S) distribution is marked in red.

The third cross-correlation peak is weakly excited because the extensions of the corresponding eigenrays do not interact with the near-surface source distribution, as already mentioned. The amplitude of the nearby second peak is possibly also affected by this weakening due to the finite bandwidth.

Even though the noise cross-correlation does not recover the full arrival pattern of Fig. 8, the cross-correlation peaks can still be used as observables. The lower panels of Fig. 9 present the CTSKs of the 3 marked peaks. While those of the first two peaks are directly comparable with the corresponding TSKs in Fig. 8, the CTSK of peak 3 reveals a different sensitivity area. This is because the last peak in the cross-correlation envelope is not an approximation of peak 3 in the arrival pattern but rather a new/different observable with a sensitivity kernel extending from the surface to deeper layers down to 500 m depth. The CTSK would be necessary in order to take advantage of the noise cross-correlation envelope in cases like this.

D. 2D CTSKs—Linear SVP—Single noise source

To mimic a localized noise source, such as a ship, a single noise source at a range of 31 km from location A (11 km from location B) is considered in the following for a

linear sound-speed profile, same as in Fig. 1(a), assuming a Gaussian receiving filter $H_1(\omega)H_2^*(\omega)$ centered at 100 Hz with 3-dB bandwidth 70 Hz. In the case of a single noise source, the time-lagged cross-correlation envelope is expected to approximate the convolution between the arrival patterns of the source at the two receivers;¹² this can also be seen from Eq. (5) where substitution of a spatial Dirac function for the space-frequency noise distribution S leads to the convolution³⁵ of the TDGF at x_1 with the time-reversed TDGF at x_2 .

Figure 10 presents the normalized 2D cross-correlation envelope and the corresponding CTSKs for a noise source depth of 10 m. The ray interference pattern between the source and the receivers at locations A and B and the corresponding eigenrays are also shown for comparison. It is seen that the cross-correlation envelope is formed about the ray interference pattern and merges nearby ray arrivals because of the finite bandwidth. The CTSKs for peaks 1 and 2 reveal that the resulting kernel is a superposition of two components, one from the source to location A, which is mostly negative, and one from the source to location B, which is mostly positive. The different signs are because of the definition of the cross-correlation in terms of the pressure at A and the conjugate pressure at B corresponding to travel-time difference, i.e., the cross-correlation peaks show the time difference of arrivals between the two receivers and so the sensitivities corresponding to the two ray paths have opposite signs. The bottom panels in Fig. 10 show the CTSKs for peaks 3 and 4. In this case, the two kernels, from the source to locations A and B, respectively, are more aligned, and they interfere in the outer region, between the noise source and location B. This sheds some light on the

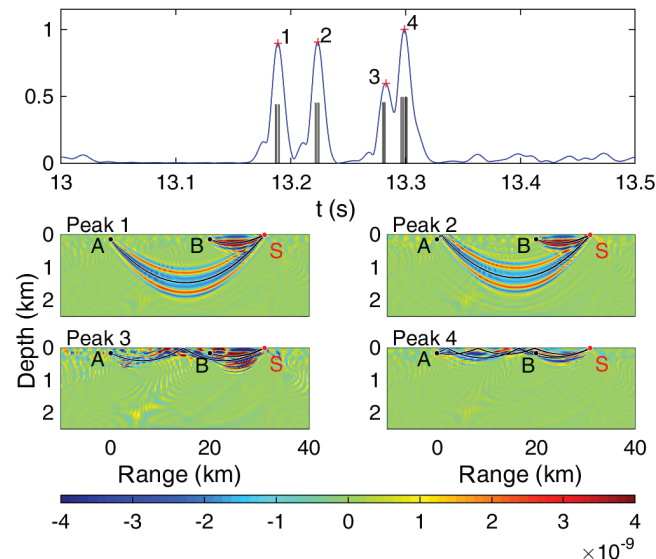


FIG. 10. Top panel: Normalized 2D wave-theoretic cross-correlation envelope and ray interference pattern at two receivers A and B located at 150-m depth in a linear SVP and separated by 20 km with Gaussian receiving filters centered at 100 Hz and with 3-dB bandwidth 70 Hz due to a single noise source (S) at 10-m depth and 31-km range. Lower panels: 2D peak-time sensitivity kernels ($s^2 m^{-3}$) for the 4 peaks marked in the top panel along with corresponding interfering eigenrays (black lines).

mechanism of sensitivity cancellation in the outer region in the case of noise source distributions, such as the ones in Fig. 3; it is because aligned kernels of opposite polarity overlap and cancel each other in the average.

Figure 11 presents the normalized 2D cross-correlation envelope and CTSKs, along with the corresponding ray interference pattern and eigenrays, for a localized noise source at 500 m depth. In this case, there are two eigenrays from the source to the receiver at B, one refracted and one refracted/surface-reflected. There was the same number of eigenrays to receiver B in the previous case (Fig. 10), but they were very close to each other due to the shallow source depth (10 m). The cross-correlation between the receptions at locations A and B results in eight significant peaks grouped in two clusters, the first corresponding to the two deep eigenrays to receiver A, and the second corresponding to the shallower ones. The CTSKs for the early peaks show the corresponding acoustic paths very clearly. On the other hand, the CTSKs for the last peaks exhibit more complicated sensitivity patterns due to overlapping of multiple acoustic paths to receiver A. Overlapping (unresolved) arrivals contribute sensitivities according to their amplitudes, and so wave-theoretic methods become important. However, the effects of small-scale structure on amplitudes^{36–38} may cause nonlinear peak-time behaviors, meaning that the CTSK, being the first (linear) term in the Taylor expansion of peak times as

a function of sound-speed perturbations, may be subject to changes due to perturbations in the sound-speed field. This is examined in the following set of numerical experiments.

E. Linearity check

To examine the validity of the CTSK-based peak-time prediction, the linear sound-speed profile of Fig. 1(a) is perturbed up to ± 2 m/s with a step of 0.2 m/s in two depth layers, first in a shallow layer between 200 and 300 m and then in a deep layer between 1450 and 1550 m. The perturbations are trapezoid-shaped—constant within the mentioned 100-m depth intervals and linearly decreasing to zero within 10 m outside. For each perturbed profile, forward calculations are performed and the corresponding noise cross-correlation envelope is obtained. The calculated normalized 2D cross-correlation envelopes between receivers A and B are shown in Fig. 12 for the case shown in Fig. 10 (a localized noise source at 10 m depth and 31 km range). The envelope corresponding to the unperturbed linear profile (perturbation amplitude 0) is the same as is shown in the top panel of Fig. 10. The larger sound-speed perturbations not only affect the peak arrival times but also change the shape of the cross-correlation envelope, with peaks fading in and out, conveying information about the changing medium beyond what can be learned from peak times alone.

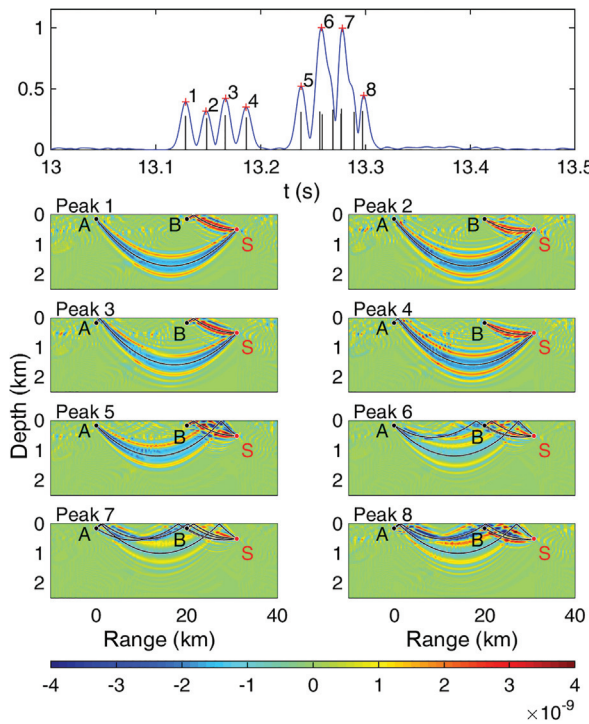


FIG. 11. Top panel: Normalized 2D wave-theoretic cross-correlation envelope and ray interference pattern for a linear SVP at two receivers A and B located at 150-m depth and separated by 20 km with Gaussian receiving filters centered at 100 Hz and with 3-dB bandwidth 70 Hz due to a single noise source (S) at 500-m depth and 31-km range. Lower panels: 2D peak-time sensitivity kernels ($s^2 m^{-3}$) for the 8 peaks marked in the top panel along with corresponding interfering eigenrays (black lines).

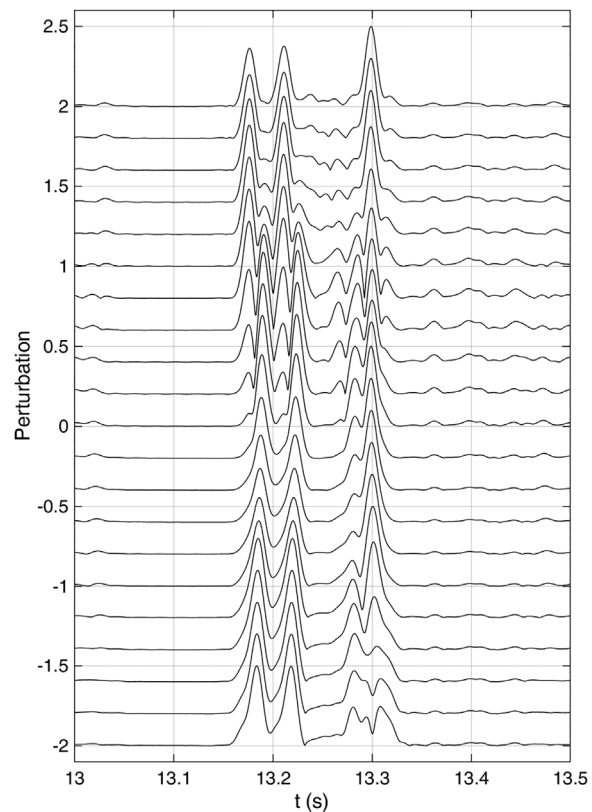


FIG. 12. Wave-theoretic 2D cross-correlation envelopes due to a noise source at 10-m depth and 31-km range for perturbations between -2 and $+2$ m/s of the linear SVP over the depth interval 200–300 m. The cross-correlation envelopes are normalized and offset by the size of the sound-speed perturbation (m/s) measured on the vertical axis.

Figure 13 shows the variations of the actual peak times (open circles) resulting from the above forward calculations and those predicted by the CTSKs (solid lines), the latter being evaluated for the unperturbed state, as functions of the sound-speed perturbation magnitude. The crosses on this figure represent the calculated ray-theoretic interference times at the two receivers. The CTSKs are equivalent to first-order derivatives of peak times with respect to the sound-speed perturbations and therefore, the CTSK predictions are straight lines tangent to the actual peak times at the unperturbed state. The actual peak times exhibit in general a non-linear behavior, and in addition, peaks fade in and out. The ray interference times exhibit similar behavior, but there are many compared to the wave-theoretic peaks, and they may be much more difficult to identify and use with real data. Remarkably, a sound-speed increase (positive perturbation) centered at 250 m causes the arrival time of early peaks to increase as well. This is because perturbations at this depth project on the positive kernel between the source and location B much more than on the negative kernel between the source and the distant location A.

Figures 14 and 15 present the normalized 2D cross-correlations and the corresponding peak times, both actual and predicted from the CTSKs, respectively, for the same noise source and perturbations of the linear sound-velocity profile centered on 1500 m depth. This time the perturbations affect

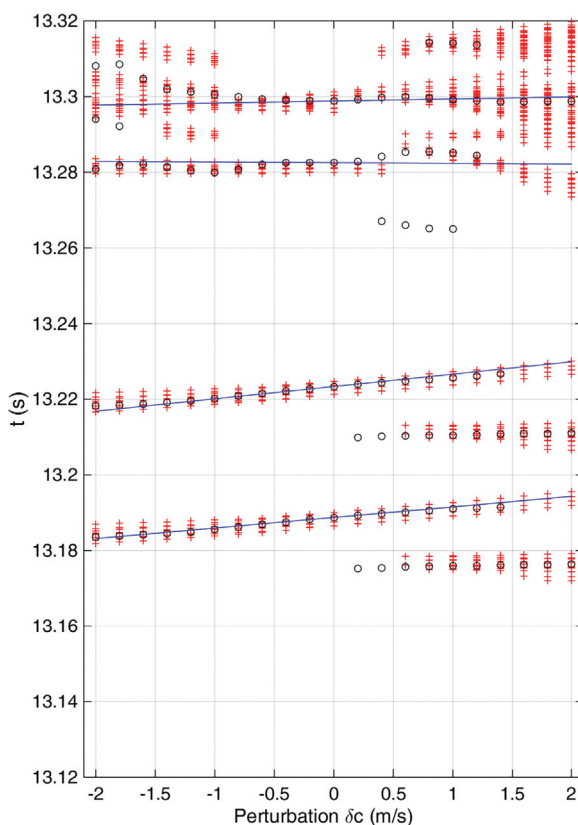


FIG. 13. Computed peak times (circles) of the cross-correlation envelopes shown in Fig. 12, ray-theoretic interference times (+) and CTSK-based predictions (lines) as functions of sound-speed perturbation amplitude for perturbations of the linear SVP over the depth interval 200–300 m.

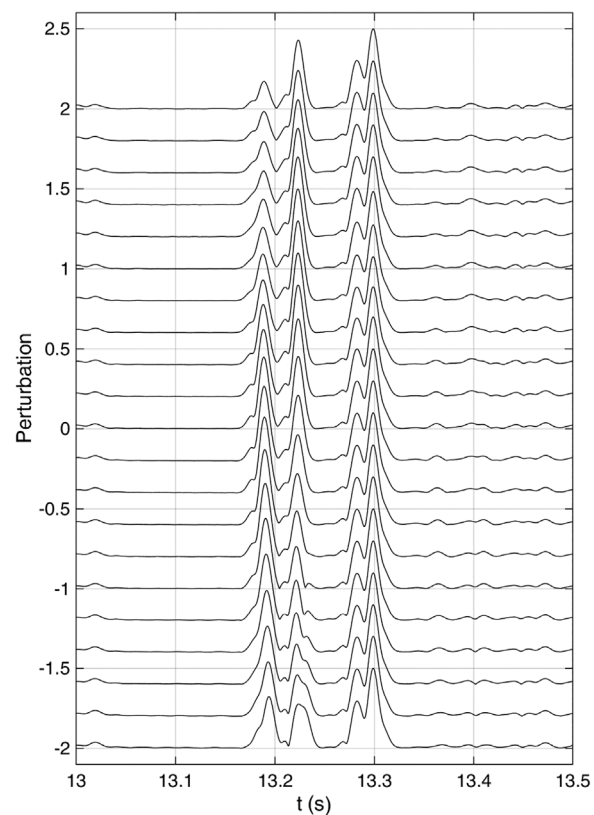


FIG. 14. Wave-theoretic 2D cross-correlation envelopes due to a noise source at 10-m depth and 31-km range for perturbations between -2 and $+2$ m/s of the linear SVP over the depth interval 1450–1550 m. The cross-correlation envelopes are normalized and offset by the size of the sound-speed perturbation (m/s) measured on the vertical axis.

the early peaks and peak times but not the late ones. This agrees with the last two CTSKs, bottom panels in Fig. 10, whose supports are at shallow depths, far from the 1500-m perturbation depth. The second arrival time shows a weak non-linear behavior for negative sound-speed perturbation values – likely because the negative sensitivity core of the corresponding CTSK marginally touches the depth of 1500 m, and the shape of the second peak changes in Fig. 14 for negative perturbations. The largest changes are observed in the first peak, both in shape (Fig. 14) and peak time (Fig. 15); it is interesting to notice that positive perturbations lead to peak weakening, whereas no interfering eigen-rays are found for perturbations larger than 0.6 m/s. The CTSK-based predictions are tangent to the actual peak times and give an approximation for the peak-time perturbations in the neighborhood of the reference state.

Calculations were also made for the noise source at 500 m (not shown). They exhibited weaker nonlinearity than for the shallow source. This is hypothesized to be because the deeper source is farther from the sound channel minimum (at the surface in this case), so the rays are generally steeper and are less likely to be nonlinear.¹³ However, the amplitudes still showed sensitivity, as the arrival peaks changed shape and the early arrivals faded out with strong positive perturbations.

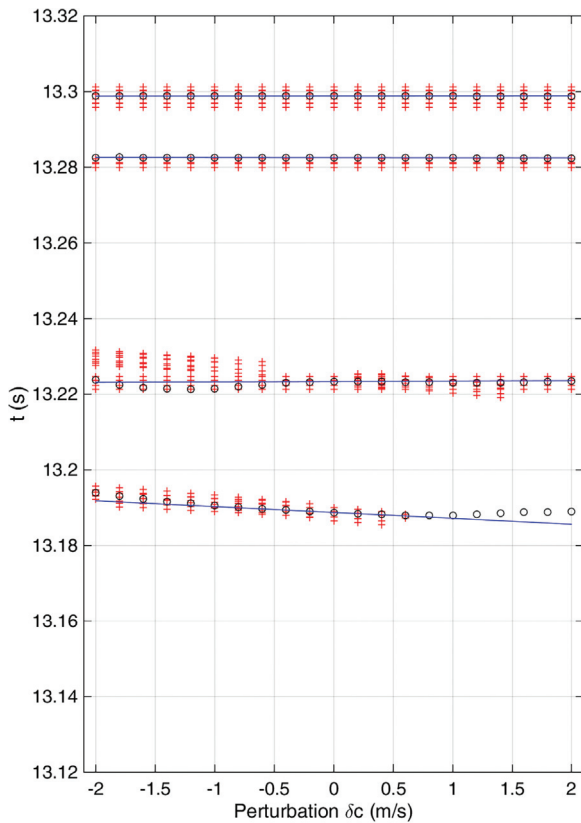


FIG. 15. Actual peak times (circles) of the cross-correlation envelopes shown in Fig. 14, ray-theoretic interference times (+), and CTSK-based predictions (lines) as functions of sound-speed perturbation amplitude for perturbations of the linear SVP over the depth interval 1450–1550 m.

IV. DISCUSSION AND CONCLUSIONS

This paper studied the sensitivity of peak times of the noise cross-correlation envelope between two locations with respect to sound-speed changes by introducing the corresponding sensitivity kernel. The cross-correlation peak-time sensitivity kernel (CTSK) is a function of the spatial variable \mathbf{x} and describes the first-order effect that a change in the sound speed at any location \mathbf{x} will have on the corresponding peak time.

Under ideal conditions, when the directivity distribution of the induced noise field spans the launch angles of all acoustic paths connecting the two receiver locations, the resulting cross-correlation envelope can be used as a proxy of the arrival pattern, the envelope of the finite-bandwidth counterpart of the time-domain Green's function between the two locations.¹² Under such conditions the perturbation behavior and the sensitivity kernels of the corresponding peak times in the cross-correlation envelope and the arrival pattern, respectively, will be close to each other, and in that respect, the CTSK would bring nothing new compared to the travel-time sensitivity kernel (TSK). This would be a case for passive tomography, in which the acoustic reception between two locations can be replaced by the noise cross-correlation envelope between these locations and TSK-based inversions can be carried out.

However, in a realistic situation, these favorable conditions should be considered to be the exception rather than the rule. In general, the induced noise directivity distribution at receiver locations will be non-uniform, because of the propagation conditions, the noise-source distribution, the receiver locations, or a combination of those, resulting in a partial stimulation of the acoustic paths connecting the two locations. In such cases, the noise cross-correlation envelope cannot be used as a proxy for the active arrival pattern, and inversions based on the TSKs cannot be carried out. Nevertheless, one might still consider estimating the ocean state using the peak times defined on the cross-correlation envelope itself as observables of their own. This would be a case for cross-correlation CTSK-based inversions.

Previous work provided a framework for a general, wave-theoretic prediction of the anticipated cross-correlation function for a given environment and distribution of noise sources,¹² and its derivative, the cross-correlation sensitivity kernel, with respect to noise source distribution.²⁴ The present work focuses on the sensitivity of the peak times defined on the cross-correlation envelope to sound-speed changes as described by the CTSK. The CTSK corresponds to the first-order (linear) term in the Taylor expansion of peak-time perturbations as a function of the underlying sound-speed perturbations about the reference state.

The support of the CTSK in general spans the volume between the noise sources and the receiver locations. This is clearly observed in the case of the 3D CTSKs for the linear noise source distribution in Sec. III B, where sound-speed perturbations not only between the two receivers but also in the outer region, between the noise sources and the receivers, appear to have a first-order effect on the cross-correlation peak times, in contrast to the 2D CTSKs where sensitivities are confined mainly between the two receivers. On the other hand, taking horizontal cross-range marginals of the 3D kernels, associated with the horizontal scales of typical ocean perturbations which are large compared to the CTSK cross-range extent, appears to suppress the sensitivity in the outer domain leaving a sensitivity in the inner domain only, comparable with the 2D sensitivity picture.

In the case of a localized noise source, the CTSK is a superposition of two components, distributed about the acoustic paths connecting the source with each of the two receivers. These two CTSK components have opposite signs associated with the definition of the cross-correlation—conjugation in the frequency domain for the pressure at one of the receivers means reversal in the time domain. Thus, the CTSK reproduces the differencing of the propagation times along the paths from the source to the two receivers. Should the noise source lie exactly on the extension of an acoustic path (eigenray) passing through the two receivers, then, the two CTSK components would perfectly overlap in the outer domain, where they would also tend to cancel out each other due to their opposite signs, leaving behind a CTSK supported in the inner region (between the two receivers) about the corresponding acoustic path.

In a diffuse noise field generated by a distribution of noise sources, the coherent arrivals at the two receivers, corresponding to acoustic energy from the same noise source(s) passing through both receivers and associated with CTSKs supported about the corresponding eigenrays, will prevail over the incoherent arrivals (corresponding to sound energy following uncorrelated paths) and will contribute to the recovery of the TDGF and the corresponding arrival pattern. In general, coherent arrivals are due to noise sources distributed about the extensions of eigenrays connecting the two receivers.

The forward calculations show that cross-correlation envelope peak times exhibit a non-linear dependence on sound-speed changes in general, and the non-linearity becomes stronger in the case of interference between nearby (unresolved) ray arrivals. In all cases, the linear predictions based on the CTSKs are tangent to the actual peak times at the reference state. The ray-theoretic calculations resulted in many peaks which are hidden and remain unresolved under the peaks of the wave-theoretic cross-correlation envelope. The lack of ray resolution due to the finite bandwidth would prevent a ray-theoretic interpretation of peak time perturbations and a corresponding environmental inversion in finite-bandwidth noise cross-correlation functions. The use of receiving arrays and the application of single or double beamforming^{39,40} would be an interesting option resulting in enhanced resolution and probably leading to an extension of linearity regimes in such cases.

Even though the reference environments and the sound-speed perturbations chosen are idealized, serving the demonstration of basic sensitivities of cross-correlation peak times, the CTSK approach presented here allows for the calculation of the linearized effect of any kind of sound-speed perturbation (e.g., range-dependent, small-scale) relative to any reference state. An effect that has not been accounted for is that of surface roughness degrading the coherence of surface bounce paths. Surface roughness is expected to affect primarily the amplitudes of the cross-correlation envelope, weakening the summing up of the acoustic energy, and reducing the precision of the peak times addressed here. Motion of the instruments or the noise sources would also affect the coherence. Receiver motion was addressed in an earlier work, but differential Doppler dilation from a moving impulsive source would also reduce the cross-correlations. The peak arrival time precision can be calculated from peak bandwidth and signal-to-noise ratio,¹³ and so weak peaks will not carry much environmental information.

ACKNOWLEDGMENTS

This work was supported by the Office of Naval Research, awards N00014-18-1-2698, N00014-19-1-263 (BC), and N62909-20-1-2084 (ES). The authors are thankful to the anonymous reviewers for their helpful comments and suggestions.

APPENDIX: ANALYTIC REPRESENTATION OF THE NOISE CROSS-CORRELATION FUNCTION

The cross-correlation function of a stationary acoustic noise field at two locations \mathbf{x}_1 and \mathbf{x}_2 is given by the expression

$$c_{1,2}(\tau) = \langle p(t + \tau; \mathbf{x}_1) p^*(t; \mathbf{x}_2) \rangle \\ = \frac{1}{2\pi} \int_{-\infty}^{\infty} \langle P(\omega; \mathbf{x}_1) P^*(\omega; \mathbf{x}_2) \rangle e^{i\omega\tau} d\omega, \quad (\text{A1})$$

where p is the time-domain and P the frequency-domain acoustic pressure due to noise. While the above expression, based on the Wiener–Khinchin theorem, involves complex formalism, the time-domain pressure p at any location \mathbf{x}_r and the resulting cross-correlation function are real-valued, meaning that the frequency-domain pressure is Hermitian: $P(\omega; \mathbf{x}_r) = P^*(-\omega; \mathbf{x}_r)$.

An analytic representation $p_a(t) = p(t) + i\tilde{p}(t)$ of the time-domain pressure $p(t)$ can be obtained through the Hilbert transform

$$\tilde{p}(t) = H_t \{ p(t) \} = \frac{1}{\pi} \int_{-\infty}^{+\infty} \frac{p(t')}{t - t'} dt'. \quad (\text{A2})$$

The Fourier transform of $\tilde{p}(t)$ is a phase-shifted version of $P(\omega)$, a basic property of the Hilbert transform:

$$\tilde{P}(\omega) = \int_{-\infty}^{\infty} \tilde{p}(t) e^{-i\omega t} dt = -i\text{sgn}(\omega) P(\omega) \\ = \begin{cases} -iP(\omega) & \text{for } \omega > 0 \\ iP(\omega) & \text{for } \omega < 0. \end{cases} \quad (\text{A3})$$

Accordingly, the Fourier transform of the analytic representation becomes

$$P_a(\omega) = \int_{-\infty}^{\infty} p_a(t) e^{-i\omega t} dt = P(\omega) + i\tilde{P}(\omega) \\ = \begin{cases} 2P(\omega) & \text{for } \omega > 0 \\ 0 & \text{for } \omega < 0, \end{cases} \quad (\text{A4})$$

i.e., it is two times the one-sided frequency-domain pressure. In that respect, the real-valued pressure can be written as

$$p(t) = \Re \{ p_a(t) \} = \frac{p_a(t) + p_a^*(t)}{2} \\ = \frac{1}{4\pi} \int_{-\infty}^{\infty} [P_a(\omega) + P_a^*(-\omega)] e^{i\omega t} d\omega. \quad (\text{A5})$$

Since $P_a(\omega)$ is one-sided, Eq. (A4), the following equation holds

$$P_a(\omega; \mathbf{x}_1) P_a(-\omega; \mathbf{x}_2) = 0, \quad (\text{A6})$$

for any circular frequency ω and any locations \mathbf{x}_1 and \mathbf{x}_2 in the field.

Using the analytic representation of the time-domain pressure, a complex-valued cross-correlation function $\psi_{1,2}(\tau)$ can be defined

$$\begin{aligned}\psi_{1,2}(\tau) &= \langle p_a(t + \tau; \mathbf{x}_1) p_a^*(t; \mathbf{x}_2) \rangle \\ &= \frac{1}{2\pi} \int_{-\infty}^{\infty} \langle P_a(\omega; \mathbf{x}_1) P_a^*(\omega; \mathbf{x}_2) \rangle e^{i\omega\tau} d\omega,\end{aligned}\quad (\text{A7})$$

with Fourier transform

$$\begin{aligned}\Psi_{1,2}(\omega) &= \langle P_a(\omega; \mathbf{x}_1) P_a^*(\omega; \mathbf{x}_2) \rangle \\ &= \begin{cases} 4 \langle P(\omega; \mathbf{x}_1) P^*(\omega; \mathbf{x}_2) \rangle & \text{for } \omega > 0 \\ 0 & \text{for } \omega < 0. \end{cases}\end{aligned}\quad (\text{A8})$$

The conjugate of $\psi_{1,2}(\tau)$ is

$$\begin{aligned}\psi_{1,2}^*(\tau) &= \langle p_a^*(t + \tau; \mathbf{x}_1) p_a(t; \mathbf{x}_2) \rangle \\ &= \frac{1}{2\pi} \int_{-\infty}^{\infty} \langle P_a^*(-\omega; \mathbf{x}_1) P_a(-\omega; \mathbf{x}_2) \rangle e^{i\omega\tau} d\omega.\end{aligned}\quad (\text{A9})$$

The real part of $\psi_{1,2}(\tau)$ can then be written as

$$\begin{aligned}\Re\{\psi_{1,2}(\tau)\} &= \frac{\psi_{1,2}(\tau) + \psi_{1,2}^*(\tau)}{2} \\ &= \frac{1}{4\pi} \int_{-\infty}^{\infty} \langle P_a(\omega; \mathbf{x}_1) P_a^*(\omega; \mathbf{x}_2) \rangle e^{i\omega\tau} d\omega \\ &\quad + \frac{1}{4\pi} \int_{-\infty}^{\infty} \langle P_a^*(-\omega; \mathbf{x}_1) P_a(-\omega; \mathbf{x}_2) \rangle e^{i\omega\tau} d\omega.\end{aligned}\quad (\text{A10})$$

On the other hand, the real-valued cross-correlation per definition (A1) and with the help of Eq. (A5) can be written as

$$\begin{aligned}c_{1,2}(\tau) &= \langle p(t + \tau; \mathbf{x}_1) p^*(t; \mathbf{x}_2) \rangle \\ &= \frac{1}{4} \left\langle [p_a(t + \tau; \mathbf{x}_1) + p_a^*(t + \tau; \mathbf{x}_1)] \right. \\ &\quad \times \left. [p_a(t; \mathbf{x}_2) + p_a^*(t; \mathbf{x}_2)]^* \right\rangle \\ &= \frac{1}{8\pi} \int_{-\infty}^{\infty} \left\langle [P_a(\omega; \mathbf{x}_1) + P_a^*(-\omega; \mathbf{x}_1)] [P_a(\omega; \mathbf{x}_2) \right. \\ &\quad \left. + P_a^*(-\omega; \mathbf{x}_2)]^* \right\rangle e^{i\omega\tau} d\omega \\ &= \frac{1}{8\pi} \int_{-\infty}^{\infty} \left\langle [P_a(\omega; \mathbf{x}_1) + P_a^*(-\omega; \mathbf{x}_1)] [P_a^*(\omega; \mathbf{x}_2) \right. \\ &\quad \left. + P_a(-\omega; \mathbf{x}_2)] \right\rangle e^{i\omega\tau} d\omega \\ &= \frac{1}{8\pi} \int_{-\infty}^{\infty} \left\langle P_a(\omega; \mathbf{x}_1) P_a^*(\omega; \mathbf{x}_2) \right\rangle e^{i\omega\tau} d\omega \\ &\quad + \frac{1}{8\pi} \int_{-\infty}^{\infty} \langle P_a^*(-\omega; \mathbf{x}_1) P_a(-\omega; \mathbf{x}_2) \rangle e^{i\omega\tau} d\omega,\end{aligned}\quad (\text{A11})$$

where Eq. (A6) was used to erase the cross-terms. By comparing expressions (A10) and (A11) it turns out that the real-valued cross-correlation is half the real part of the complex-valued cross-correlation

$$c_{1,2}(\tau) = \frac{1}{2} \Re\{\psi_{1,2}(\tau)\}. \quad (\text{A12})$$

A. Cross-correlation envelope

The complex-valued cross-correlation function allows for the straightforward calculation of the cross-correlation envelope as the modulus of $\psi_{1,2}(\tau)$

$$c_E(\tau) = |\psi_{1,2}(\tau)|. \quad (\text{A13})$$

Alternatively, the cross-correlation envelope can be calculated as the modulus of the analytic representation $c_{1,2}^{(a)}(\tau) = c_{1,2}(\tau) + i\tilde{c}_{1,2}(\tau)$ of the real-valued cross-correlation function $c_{1,2}(\tau)$, $c_E(\tau) = \sqrt{c_{1,2}^2(\tau) + \tilde{c}_{1,2}^2(\tau)}$, where the imaginary part $\tilde{c}_{1,2}(\tau)$ is obtained through the Hilbert transform

$$\tilde{c}_{1,2}(\tau) = H_\tau\{c_{1,2}(\tau)\} = \frac{1}{\pi} \int_{-\infty}^{+\infty} \frac{c_{1,2}(\tau')}{\tau - \tau'} d\tau'. \quad (\text{A14})$$

The Fourier transform of $c_{1,2}(\tau)$ is given by Eq. (A11),

$$\begin{aligned}C_{1,2}(\omega) &= \frac{1}{4} \langle P_a(\omega; \mathbf{x}_1) P_a^*(\omega; \mathbf{x}_2) \rangle \\ &\quad + \frac{1}{4} \langle P_a^*(-\omega; \mathbf{x}_1) P_a(-\omega; \mathbf{x}_2) \rangle.\end{aligned}\quad (\text{A15})$$

The Fourier transform of $\tilde{c}_{1,2}(\tau)$ is a phase-shifted version of $C_{1,2}(\omega)$,

$$\begin{aligned}\tilde{C}_{1,2}(\omega) &= \int_{-\infty}^{\infty} \tilde{c}_{1,2}(\tau) e^{-i\omega\tau} d\tau = -i\text{sgn}(\omega) C_{1,2}(\omega) \\ &= \begin{cases} -iC_{1,2}(\omega) & \text{for } \omega > 0 \\ iC_{1,2}(\omega) & \text{for } \omega < 0. \end{cases}\end{aligned}\quad (\text{A16})$$

Accordingly, the Fourier transform of $c_{1,2}^{(a)}(\tau)$ becomes

$$\begin{aligned}C_{1,2}^{(a)}(\omega) &= \int_{-\infty}^{\infty} c_{1,2}^{(a)}(\tau) e^{-i\omega\tau} d\tau = C_{1,2}(\omega) + i\tilde{C}_{1,2}(\omega) \\ &= \begin{cases} 2C_{1,2}(\omega) & \text{for } \omega > 0 \\ 0 & \text{for } \omega < 0,\end{cases}\end{aligned}\quad (\text{A17})$$

which by virtue of Eqs. (A15) and (A4), i.e., taking into account that $P_a(\omega)$ is one-sided and that for $\omega > 0$ $P_a(-\omega)$ vanishes, becomes

$$C_{1,2}^{(a)}(\omega) = \frac{1}{2} \langle P_a(\omega; \mathbf{x}_1) P_a^*(\omega; \mathbf{x}_2) \rangle = \frac{1}{2} \Psi_{1,2}(\omega). \quad (\text{A18})$$

Going back to the time-lag domain, this relation becomes

$$c_{1,2}^{(a)}(\tau) = \frac{1}{2} \psi_{1,2}(\tau). \quad (\text{A19})$$

This is the generalization of Eq. (A12). The above relations indicate that the cross-correlation envelope can be obtained in two alternative ways:

- (1) As the modulus of the analytic representation $c_{1,2}^{(a)}(\tau)$ of the cross-correlation function $c_{1,2}(\tau)$ resulting from the real-valued pressure $p(t)$.
- (2) As the modulus of the complex-valued cross-correlation $\psi_{1,2}(\tau)$ resulting from the analytic pressure $p_a(t)$ based on the one-sided Green's function.

The two ways are equivalent.

- ¹O. I. Lobkis and R. L. Weaver, "On the emergence of the Green's function in the correlations of a diffuse field," *J. Acoust. Soc. Am.* **110**, 3011–3017 (2001).
- ²P. Roux, W. A. Kuperman, and the NPAL Group, "Extracting coherent wavefronts from acoustic ambient noise in the ocean," *J. Acoust. Soc. Am.* **116**, 1995–2003 (2004).
- ³R. L. Weaver and O. I. Lobkis, "Fluctuations in diffuse field-field correlations and the emergence of the Green's function in open systems," *J. Acoust. Soc. Am.* **117**, 3432–3439 (2005).
- ⁴K. G. Sabra, P. Roux, and W. A. Kuperman, "Arrival structure of the time-averaged ambient noise cross-correlation function in an oceanic waveguide," *J. Acoust. Soc. Am.* **117**, 164–174 (2005).
- ⁵P. Roux, K. G. Sabra, W. A. Kuperman, and A. Roux, "Ambient noise cross-correlation in free space: Theoretical approach," *J. Acoust. Soc. Am.* **117**, 79–84 (2005).
- ⁶O. A. Godin, "Recovering the acoustic Green's function from ambient noise cross-correlation in an inhomogeneous moving medium," *Phys. Rev. Lett.* **97**, 054301 (2006).
- ⁷O. Godin, "Cross-correlation function of acoustic fields generated by random high-frequency sources," *J. Acoust. Soc. Am.* **128**, 600–610 (2010).
- ⁸N. Zabotin and O. Godin, "Emergence of acoustic Green's functions from time averages of ambient noise," *Acta Acustica* **97**, 44–53 (2011).
- ⁹O. A. Godin, "Acoustic noise interferometry in a time-dependent coastal ocean," *J. Acoust. Soc. Am.* **143**, 595–604 (2018).
- ¹⁰K. G. Sabra, P. Roux, and W. A. Kuperman, "Emergence rate of the time-domain Green's function from the ambient noise cross-correlation function," *J. Acoust. Soc. Am.* **118**, 3524–3531 (2005).
- ¹¹C. Leroy, S. Lani, K. G. Sabra, W. Hodgkiss, W. A. Kuperman, S. Walker, and P. Roux, "Enhancing the emergence rate of coherent wavefronts from ambient shipping noise correlations using spatio-temporal filters," *J. Acoust. Soc. Am.* **132**, 883–893 (2012).
- ¹²E. K. Skarsoulis and B. D. Cornuelle, "Cross-correlation of shipping noise: Refraction and receiver-motion effects," *J. Acoust. Soc. Am.* **145**, 3003–3010 (2019).
- ¹³W. H. Munk, P. F. Worcester, and C. Wunsch, *Ocean Acoustic Tomography* (Cambridge University Press, New York, 1995).
- ¹⁴E. K. Skarsoulis and B. D. Cornuelle, "Travel-time sensitivity kernels in ocean acoustic tomography," *J. Acoust. Soc. Am.* **116**, 227–238 (2004).
- ¹⁵M. A. Dzieciuch, B. D. Cornuelle, and E. K. Skarsoulis, "Structure and stability of wave-theoretic kernels in the ocean," *J. Acoust. Soc. Am.* **134**, 3318–3331 (2013).
- ¹⁶S. Lani, K. G. Sabra, W. S. Hodgkiss, W. A. Kuperman, and P. Roux, "Coherent processing of shipping noise for ocean monitoring," *J. Acoust. Soc. Am.* **133**, EL108–EL113 (2013).
- ¹⁷M. G. Brown, O. A. Godin, X. Zang, J. S. Ball, N. A. Zabotin, L. Y. Zabotina, and N. J. Williams, "Ocean acoustic remote sensing using ambient noise: Results from the Florida Straits," *Geophys. J. Int.* **206**, 574–589 (2016).
- ¹⁸K. F. Woolfe, S. Lani, K. G. Sabra, and W. A. Kuperman, "Monitoring deep-ocean temperatures using acoustic ambient noise," *Geophys. Res. Lett.* **42**, 2878–2884, <https://doi.org/10.1002/2015GL063438> (2015).
- ¹⁹K. F. Woolfe and K. G. Sabra, "Variability of the coherent arrivals extracted from low-frequency deep-ocean ambient noise correlations," *J. Acoust. Soc. Am.* **138**, 521–532 (2015).
- ²⁰W. A. Kuperman and F. Ingenito, "Spatial correlation of surface generated noise in a stratified ocean," *J. Acoust. Soc. Am.* **67**, 1988–1996 (1980).
- ²¹M. J. Buckingham, "On surface-generated ambient noise in an upward refracting ocean," *Philos. Trans. R. Soc. London A* **346**, 321–352 (1994).
- ²²M. J. Buckingham, "On the two-point cross-correlation function of anisotropic, spatially homogeneous ambient noise in the ocean and its relationship to the Green's function," *J. Acoust. Soc. Am.* **129**, 3562–3576 (2011).
- ²³M. J. Buckingham, "Cross-correlation in band-limited ocean ambient noise fields," *J. Acoust. Soc. Am.* **131**, 2643–2657 (2012).
- ²⁴E. K. Skarsoulis and B. D. Cornuelle, "Cross-correlation sensitivity kernels with respect to noise source distribution," *J. Acoust. Soc. Am.* **147**, 1–9 (2020).
- ²⁵W. A. Gardner, *Introduction to Random Processes: With Applications to Signals and Systems* (McGraw-Hill, New York, 1990).
- ²⁶W. G. Price and R. E. D. Bishop, *Probabilistic Theory of Ship Dynamics* (Chapman & Hall, London, 1974).
- ²⁷M. Born, "Quantenmechanik der Stoßvorgänge" ("Quantum mechanics of impact processes"), *Z. Phys.* **38**, 803–827 (1926).
- ²⁸J. R. Taylor, *Scattering Theory* (Wiley, New York, 1972).
- ²⁹G. A. Athanassoulis and E. K. Skarsoulis, "Arrival-time perturbations of broadband tomographic signals due to sound-speed disturbances. A wave-theoretic approach," *J. Acoust. Soc. Am.* **97**, 3575–3588 (1995).
- ³⁰F. B. Jensen, W. A. Kuperman, M. B. Porter, and H. Schmidt, *Computational Ocean Acoustics* (Springer Verlag, AIP Press, New York, 2000), pp. 258–276.
- ³¹M. B. Porter and E. L. Reiss, "A numerical method for ocean acoustic normal modes," *J. Acoust. Soc. Am.* **76**, 244–252 (1984).
- ³²E. K. Skarsoulis, B. D. Cornuelle, and M. A. Dzieciuch, "Travel-time sensitivity kernels in long-range propagation," *J. Acoust. Soc. Am.* **126**, 2223–2233 (2009).
- ³³H. Marquering, G. Nolet, and F. A. Dahlen, "Three-dimensional waveform sensitivity kernels," *Geophys. J. Int.* **132**, 521–534 (1998).
- ³⁴H. Marquering, F. A. Dahlen, and G. Nolet, "Three-dimensional sensitivity kernels for finite-frequency traveltimes: The banana-doughnut paradox," *Geophys. J. Int.* **137**, 805–815 (1999).
- ³⁵R. N. Bracewell, *The Fourier Transform and Its Applications* (McGraw-Hill, Singapore, 1965).
- ³⁶M. G. Brown, "A Maslov-Chapman wavefield representation for wide-angle one-way propagation," *Geophys. J. Int.* **116**, 513–526 (1994).
- ³⁷J. Sarkar, B. D. Cornuelle, and W. A. Kuperman, "Information and linearity of time-domain complex demodulated amplitude and phase data in shallow water," *J. Acoust. Soc. Am.* **130**, 1242–1252 (2011).
- ³⁸J. A. Colosi, *Sound Propagation through the Stochastic Ocean* (Cambridge University Press, New York, 2016).
- ³⁹P. Roux, B. D. Cornuelle, W. A. Kuperman, and W. S. Hodgkiss, "The structure of raylike arrivals in a shallow-water waveguide," *J. Acoust. Soc. Am.* **124**, 3430–3439 (2008).
- ⁴⁰F. Aulanier, B. Nicolas, P. Roux, and J. I. Mars, "Time-angle sensitivity kernels for sound-speed perturbations," *J. Acoust. Soc. Am.* **134**, 88–96 (2013).